

RESEARCH ARTICLE

10.1002/2016JD025793

Special Section:

Quantifying the emission, properties, and diverse impacts of wildfire smoke

Key Points:

- GESO-Chem model with nested grid capability and FINN emission shows smoke transport from Southeast Asia to Southwest China
- Simulated AOD temporal variability agrees with that from the limited but first-ever ground observations in the region
- Northeast India and Burma are the largest contributor to smoke aerosol in Southwest China

Correspondence to:

X. Xia and J. Wang,
xxa@mail.iap.ac.cn;
jun-wang-1@uiowa.edu

Citation:

Zhu, J., X. Xia, J. Wang, J. Zhang, C. Wiedinmyer, J. A. Fisher, and C. A. Keller (2017), Impact of Southeast Asian smoke on aerosol properties in Southwest China: First comparison of model simulations with satellite and ground observations, *J. Geophys. Res. Atmos.*, 122, 3904–3919, doi:10.1002/2016JD025793.

Received 24 AUG 2016

Accepted 7 MAR 2017

Accepted article online 13 MAR 2017

Published online 1 APR 2017

Impact of Southeast Asian smoke on aerosol properties in Southwest China: First comparison of model simulations with satellite and ground observations

Jun Zhu^{1,2,3,4} , Xiangao Xia^{2,4} , Jun Wang^{3,5} , Jinqiang Zhang^{2,4}, Christine Wiedinmyer⁶ , Jenny A. Fisher^{7,8} , and Christoph A. Keller⁹ 

¹Collaborative Innovation Center on Forecast and Evaluation of Meteorological Disasters, Key Laboratory for Aerosol-Cloud-Precipitation of China Meteorological Administration, Nanjing University of Information Science and Technology, Nanjing, China, ²LAGEO, Institute of Atmospheric Physics, Chinese Academy of Sciences, Beijing, China, ³EAS, University of Nebraska–Lincoln, Lincoln, Nebraska, USA, ⁴College of Earth Sciences, University of Chinese Academy of Sciences, Beijing, China, ⁵Center of Global and Regional Environmental Research and Department of Chemical and Biochemical Engineering, University of Iowa, Iowa City, Iowa, USA, ⁶National Center for Atmospheric Research, Boulder, Colorado, USA, ⁷Centre for Atmospheric Chemistry, School of Chemistry, University of Wollongong, Wollongong, New South Wales, Australia, ⁸School of Earth and Environmental Sciences, University of Wollongong, Wollongong, New South Wales, Australia, ⁹School of Engineering and Applied Sciences, Harvard University, Cambridge, Massachusetts, USA

Abstract Smoke aerosols have been observed in Southwest China as a result of long-range transport from surrounding areas in March and April. The processes driving this transport and the resultant impact on regional aerosol optical properties are studied here through a combined use of the Goddard Earth Observing System (GEOS)-Chem chemistry transport model in conjunction with satellite and the first-ever ground-based observations in the Southwest China. The potential biomass burning source regions as well as their respective contributions to aerosol loading in Southwest China are quantified. Compared to Sun photometer observations of aerosol optical depth (AOD) at 550 nm at eight stations in the study region (10–28°N, 90–115°E, comprising Northeast India, Indo-China Peninsula, and Southwest and South China), the AOD simulated by GEOS-Chem (nested grid with 0.5° × 0.667° resolution) by using the Fire Inventory from National Center for Atmospheric Research shows an average bias of –0.17 during January 2012 to May 2013. However, during the biomass burning months (March–April), the simulated AOD is much improved with a bias of –0.04. Model sensitivity experiments show that biomass burning in Burma and Northeast India is the largest contributor to smoke AOD (~88%) and total AOD (~57%) over Kunming, an urban site in Southwest China. Case studies on 21–23 March 2013 show that the smoke layer in Northeast India and North Burma can extend from the surface to 4 km and then be transported to Southwest China by prevailing westerly airflow. Model-simulated AOD and vertical distribution of aerosols are respectively in good agreement with satellite measurements from Moderate Resolution Imaging Spectroradiometer and Cloud-Aerosol Lidar with Orthogonal Polarization.

1. Introduction

Biomass burning (BB) is an important source of many trace gases and aerosol particles in the atmosphere [Crutzen and Andreae, 1990]. According to the Emissions Database for Global Atmospheric Research (EDGAR), BB produces 51% of global carbon monoxide (CO) emissions and 20% of nitrogen oxides (NO_x) emissions [Olivier *et al.*, 2005] and accounts for 42% of particulate black carbon (BC) emissions and 74% of particulate organic carbon (OC) emissions among global combustion sources [Bond *et al.*, 2004]. Smoke aerosols from BB can degrade the visibility and air quality in both source and downwind regions [Pepler *et al.*, 2000] and have important impacts on climate and weather by scattering and absorbing radiation and by aerosol-cloud interaction [Twomey, 1977; Penner *et al.*, 1992; International Panel on Climate Change, 2013]. Furthermore, the BC in BB aerosol can heat the air via strong absorption, modify regional atmospheric stability and vertical motions, and affect the large-scale circulation and hydrologic cycle [Jacobson, 2001; Menon *et al.*, 2002]. The accuracy of aerosol radiative forcing, especially aerosol-cloud interactions, is important for understanding climate change. To reduce the uncertainty in aerosol radiative effects from smoke, we first need to understand smoke aerosol long-range transport.

The impacts of smoke transport have attracted much attention and have been studied extensively in many parts of the world, including central America [Wang and Christopher, 2006; Wang et al., 2006; Saide et al., 2015], Russia [Damoah et al., 2004; Mielonen et al., 2012; Péré et al., 2014], and Africa [Ansmann et al., 2009; Williams et al., 2012; Yang et al., 2013]. BB is known to be an important contributor to air pollution in Asia [Streets et al., 2003; Aouizerats et al., 2015]. BB in South and Southeast Asia is responsible for a large component of the atmospheric brown cloud [Ramanathan et al., 2007; Stone et al., 2007] and can contribute to the formation of regional-scale haze [Engling and Gelencser, 2010; Engling et al., 2014]. Previous results indicated that BB in South and Southeast Asia significantly impacts downwind regions, such as South China [Chan et al., 2003; Huang et al., 2013; Lin et al., 2014], the northwestern Pacific [Jacob et al., 2003], and the central Tibetan Plateau [Xia et al., 2011]. Engling et al. [2011] estimated the impacts of BB from Southeast Asia on the concentrations of BC and particulate matter in Southwest China by using aerosol chemical measurements, the Moderate Resolution Imaging Spectroradiometer (MODIS) fire products, and back trajectories. Our study intends to make the first attempt to analyze the processes responsible for smoke transport to Southwest China and their impact on local aerosol optical properties by combining a chemistry transport model with satellite and ground-based observations.

The Yunnan-Guizhou Plateau or Yungui Plateau (YGP), located in Southwest China, is one of the four major Plateaus in China. The elevation of YGP is generally larger than 2000 m with mountain peaks as high as 3700 m. Due to the high elevation and the low latitude, the climate there is characterized by yearlong intense solar radiation with large diurnal variation, small monthly variations in temperature, and two distinct seasons: the wet season (May–October) and the dry season (November–April). The YGP borders the Indo-China Peninsula (ICP), which mainly includes Burma, Vietnam, Laos, Cambodia, and Thailand, and it lies to the east of Northeast India. All of these surrounding regions are characterized by frequent BB in the late dry season [Streets et al., 2003]. Our previous study revealed that aerosol optical depth (AOD) in YGP was likely influenced by the long-range transport of smoke aerosol from ICP in March and April based on analysis of Sun photometer and satellite aerosol products [Zhu et al., 2016]. Potential long-range transport of BB plumes to YGP may exert direct effects on local air quality. Furthermore, it may significantly impact surface solar radiation via biomass burning aerosol's direct and indirect radiative effects, which thereby indirectly affects availability of solar energy and carbon cycling. Therefore, further study of this issue is of significance for air quality and climate change as well as ecosystem feedbacks. There are two basic questions concerning long-range transport of BB aerosols to the YGP region that need investigation. First, which region is the major contributor of BB aerosols into the YGP? Second, what fraction of the aerosol in the YGP derives from long-range transport from BB sources during the BB months? Ground and satellite remote sensing products may provide some clues to these questions (as used in our past studies), but model simulations are required to quantitatively address these questions.

This study differs from past studies in that a chemistry transport model, for the first time, is used to analyze the process of smoke transport from Southeast Asia to Southwest China, and the model simulation is evaluated by satellite data and the first-ever ground-based observation data taken in YGP. The paper is organized as follows. We describe the observation data and model in sections 2 and 3, respectively. The results of model evaluation and the analysis of smoke aerosol transport are presented in section 4. The conclusions are presented in section 5.

2. Research Region, Data, and Methodology

The area studied is within 10–28°N and 90–115°E (comprising Northeast India, ICP, and Southwest and South China), which is separated into following subregions: the YGP (100–105°E and 22–28°N), South China (SC, 105–115°E and 22–28°N), eastern ICP (EICP, 100–110°E and 10–22°N), and western ICP (WICP, 90–100°E and 10–28°N). The specific boundaries of these regions are shown in Figure 1.

2.1. Ground Remote Sensing Data

Aerosol properties from ground-based Sun photometer measurements during March 2012 to August 2013 at Kunming (KM), an urban site in YGP, are used in the analysis. Aerosol data during January 2012 to May 2013 at seven Aerosol Robotic Network (AERONET) [Holben et al., 1998] (<http://aeronet.gsfc.nasa.gov>) stations located in the research area are also used to compare with the model simulations, including Hong_Kong_Sheung (HK), Zhongshan_Univ (ZU), Vientiane (VT), Luang_Namtha (LN), NGHIA_DO (ND), Chiang_Mai_Met_Sta

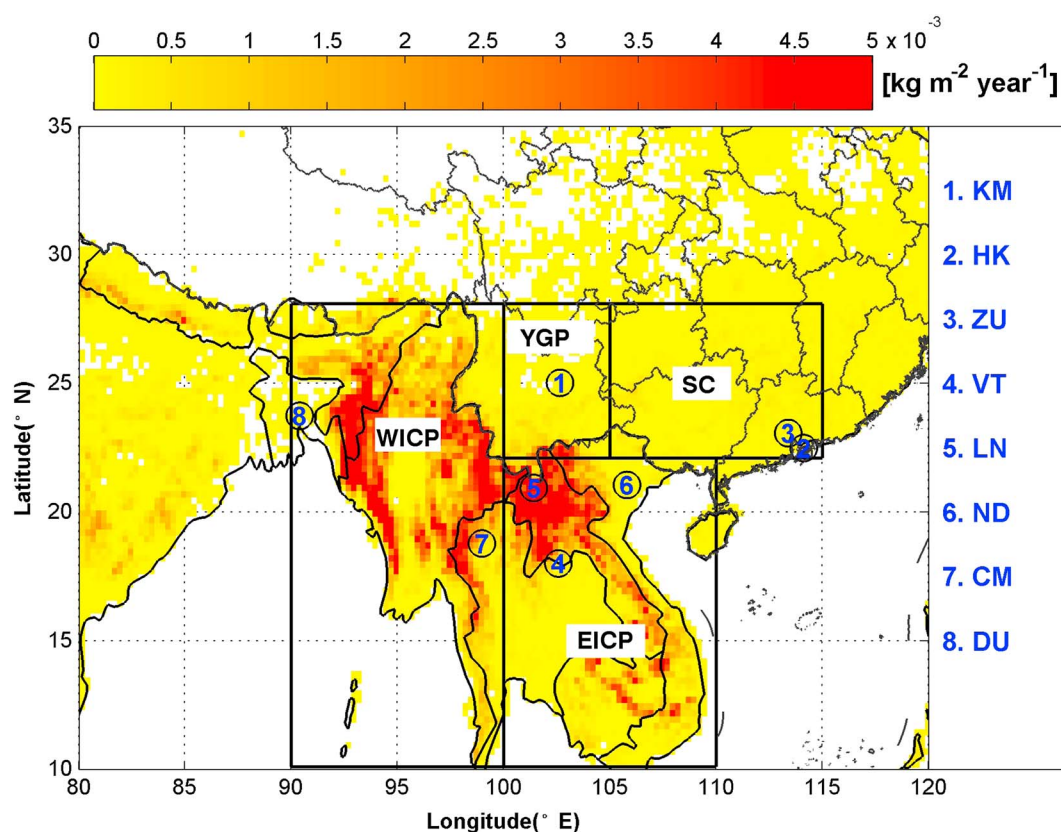


Figure 1. BC and OC emissions ($\text{kg m}^{-2} \text{yr}^{-1}$) from FINN inventory as implemented in GEOS-Chem during March–April 2004–2013. The site locations and regional classification are also shown here (YGP = Yungui Plateau, SC = South China, EICP = Eastern Indo-China Peninsula, WICP = Western Indo-China Peninsula).

(CM), and Dhaka_University (DU). Data from at least one site in each region are applied. The locations of these observational sites are specified in Table 1 and labeled in Figure 1.

AOD is the main aerosol parameter used to assess model performance. AOD is calculated from spectral solar irradiance at eight wavelengths ranging from 340 nm to 1020 nm measured by the CE318 Sun photometer (CE318), the standard instrument for AERONET. The accuracy of AOD from AERONET level 2 data is estimated to be 0.01–0.02 [Holben et al., 1998; Eck et al., 1999]. AOD at 550 nm is interpolated from AOD at 440 nm and 675 nm according to Ångström [1929].

2.2. Satellite Data

Satellite products used in this study include the Moderate Resolution Imaging Spectroradiometer (MODIS) active fires and AOD products. MODIS, onboard the NASA Terra and Aqua satellites, is a radiometer with 36 channels covering various atmospheric window and water absorption channels in 0.4–15 μm . Terra and

Table 1. Regional Division, Sites, and Locations of Eight CE318 Sun Photometer Stations

Region	Site Name	Site Location	Lon (°E)	Lat (°N)	Height (m)
Yungui Plateau (YGP)	KM	Kunming, Southwest China	102.65	25.01	1889
South China (SC)	HK	Hong_Kong_Sheung, South China	114.117	22.483	40
	ZU	Zhongshan_Univ, South China	113.390	23.060	27
Eastern Indo-China Peninsula (EICP)	VT	Vientiane, Thailand, near Vientiane (Laos)	102.570	17.992	170
	LN	Luang_Namtha, Laos	101.416	20.931	557
Western Indo-China Peninsula (WICP)	ND	NGHIA_DO, Vietnam	105.800	21.048	40
	CM	Chiang_Mai_Met_Sta, Thailand	98.972	18.771	312
	DU	Dhaka_University, Bangladesh	90.398	23.728	34

Aqua are polar-orbiting satellites that orbit the Earth in morning descending and afternoon ascending directions, respectively. The MODIS true-color images of Terra and Aqua, fire location product (<ftp://fuoco.geog.umd.edu>), and Deep-Blue/Dark-Target combined AOD at 550 nm data of Collection 6.0 [Levy *et al.*, 2013] from Aqua are used to identify smoke aerosol transport. Comparing to ground-based observation at the KM site, MODIS AOD root-mean-square error was estimated to be 0.13 and the percentage of MODIS AOD within the expected error is larger than 71% [Zhu *et al.*, 2016]. As for active fire position products, only the fire pixels with high confidence (100%) are used.

Aerosol vertical profiles from the Cloud-Aerosol Lidar with Orthogonal Polarization (CALIOP) instrument are also used in this study. CALIOP is a two-wavelength (532 nm and 1064 nm), polarization-sensitive (at 532 nm) active lidar aboard the Cloud-Aerosol Lidar and Infrared Pathfinder Satellite Observation (CALIPSO) satellite, which was launched in 2006 [Winker *et al.*, 2010]. The data used in this study include CALIOP level 1B products and level 2 aerosol profile and vertical feature mask products, which are available from the Langley Atmospheric Science Data Center (ASDC). The parameters include the attenuated backscattering coefficient profiles at 532 nm from level 1B, particulate extinction coefficient profiles at 532 nm, and vertical feature mask data products of aerosol subtype from level 2 products under 8 km height. The CALIOP AOD profile is calculated by multiplying the CALIOP particle extinction coefficient with the level thickness.

2.3. Back Trajectories

Back trajectories for the case study (21–23 March 2013) are calculated by using the Hybrid Single-Particle Lagrangian Integrated Trajectory model [Draxler and Hess, 1998] with Global Data Assimilation System one-degree archived meteorological fields. Seventy-two-hour back trajectories ending at the KM site at 2000 m, 3000 m, and 4000 m asl at 00 UTC on 21–23 March 2013 are used to identify the air mass sources. The National Centers for Environmental Prediction (NCEP) reanalysis data of surface wind and 500 Mb geopotential height on 21–23 March 2013 were downloaded from the Earth System Research Laboratory website (<http://www.esrl.noaa.gov/>) [Kalnay *et al.*, 1996].

3. Model Descriptions and Sensitivity Experiment Designs

3.1. GEOS-Chem Model

The GEOS-Chem three-dimensional chemical transport model [Bey *et al.*, 2001] version 10-01 is used to simulate aerosol optical properties on a regional scale. Here we use the nested-grid capability of GEOS-Chem with a $0.5^\circ \times 0.667^\circ$ horizontal resolution over East Asia domain (70°E – 150°E , 11°S – 55°N) and with simulation type of full chemistry (NO_x - O_x -hydrocarbon-aerosol). The nested-grid model runs are driven by Goddard Earth Observing System version 5 (GEOS-5) meteorological reanalysis fields on 47 layer vertical grid up to 0.01 hPa. The time-varying boundary conditions for the nested-grid domain are from a global GEOS-Chem simulation run at $2^\circ \times 2.5^\circ$ spatial resolution [Wang, 2004; Chen *et al.*, 2009]. GEOS-Chem uses the TPCORE advection algorithm of Lin and Rood [1996]. Convective transport was computed from the convective mass fluxes in the meteorological fields, as described by Wu *et al.* [2007]. Boundary layer mixing in GEOS-Chem uses the nonlocal scheme implemented by Lin and McElroy [2010]. Dry deposition was based on Wesely [1989] as implemented by Wang *et al.* [1998]. Wet deposition was as described by Liu *et al.* [2001].

The GEOS-Chem model has been widely used to study the impact of long-range transport on chemical composition [e.g., Jaffe *et al.*, 2004; Fairlie *et al.*, 2007; Chen *et al.*, 2009; Liu *et al.*, 2010]. However, the validation of AOD simulated by GEOS-Chem, especially in Southeast Asia, is very limited. Most previous GEOS-Chem studies have used the Global Fire Emission Database [van der Werf *et al.*, 2010] to specify emissions from fire. To cover the research period in this study, we implement the Fire Inventory from NCAR (FINN) [Wiedinmyer *et al.*, 2011] into the GEOS-Chem model by using Harvard-NASA Emission Component (HEMCO) module [Keller *et al.*, 2014]. This inventory provides high temporal (daily), spatial resolution (1 km), global estimates of a large amount of species emitted from open burning of biomass, which includes wildfire, agriculture fires, and prescribed burning but does not include biofuel use and trash burning [Wiedinmyer *et al.*, 2011]. HEMCO handles the biomass burning emissions starting from CO_2 emissions for six different land types: Savanna grasslands, woody Savannah, tropical forest,

Table 2. Model Sensitivity Experiments

Model Experiment	Short Name	Experiment Description
Experiment 1	Exp1	Include global fire emission
Experiment 2	Exp2	No fire emission
Experiment 3	Exp3	No fire emission in Yungui Plateau (YGP) subregion
Experiment 4	Exp4	No fire emission in South China (SC) subregion
Experiment 5	Exp5	No fire emission in Eastern ICP (EICP) subregion
Experiment 6	Exp6	No fire emission in Western ICP (WICP) subregion

temperate forest, boreal forest, and crops. The emissions of other gas-phase and aerosol species and nonmethane organic compounds used in GEOS-Chem are converted from CO₂ emissions by using emission ratios from *Akagi et al.* [2011] and *Yokelson et al.* [2013]. Figure 1 shows the BC and OC emissions calculated from FINN as implemented in GEOS-Chem during March–April for 10 years (2004–2013). Large emissions are observed in Burma, Laos, and Vietnam.

Global anthropogenic emissions of CO, NO_x, SO₂, and NH₃ are obtained from the EDGAR v4.2 global inventory [EC-JRC/PBL, 2009], and their distribution over Asia is overwritten by emissions from *Zhang et al.* [2009]. Biofuel emissions are from *Yevich and Logan* [2003], which contains CO, ALK4 (lumped \geq C4 alkanes), acetone, methyl ethyl ketone, acetaldehyde, PRPE (lumped \geq C3 alkenes), C₃H₈, CH₂O, and NO emissions. Anthropogenic nonmethane volatile organic compound emissions are from REanalysis of the TROpospheric chemical composition inventory [Hu et al., 2015]. Global anthropogenic emissions for carbonaceous aerosols (BC/OC) are from *Bond et al.* [2007] as implemented by *Leibensperger et al.* [2012]. The anthropogenic aircraft inventory is generated from the Aircraft Emissions Inventory Code [Stettler et al., 2011], which contains fuel burned, NO, CO, and hydrocarbons. Global ship emissions of CO are from the International Comprehensive Ocean-Atmosphere Data Set inventory [Wang et al., 2008], as implemented by *Lee et al.* [2011]. Volcanic SO₂ emissions are from AEROCOM data (http://www-lscedods.cea.fr/aerocom/AEROCOM_HC/) as implemented by *Fisher et al.* [2011]. Dust scheme used in GEOS-Chem is described in *Fairlie et al.* [2007].

3.2. Model Experiment Designs

Model simulations were conducted for January 2012 through May 2013 with 1 month spin up. AOD at 550 nm was archived every 3 h for six aerosol types: sulfate (sulfate + nitrate + ammonium), BC, OC, accumulation mode sea salt, coarse mode sea salt, and dust aerosol. Total AOD values for each vertical model layer were generated by assuming an external mixture of aerosols and summed over all aerosol types [Drury et al., 2008]. The model-simulated AOD is compared with the observed AOD from the ground-based Sun photometers at eight stations. The mean values of Sun photometer AOD data within ± 1.5 h of the model output times are matched with the AOD output of the model grid in which the site is located.

Model sensitivity experiments were conducted for March–April 2013, the late dry season when BB events occur more frequently in Southeast Asia [Pochanart, 2003]. The objective of these experiments was to explore the influence of BB emissions from each subregion on the observed aerosol at KM station during the months with high BB. Six numerical experiments were performed: experiment 1 (Exp1) includes global fire emission; experiment 2 (Exp2), no fire emission; and experiments 3–6 (Exp3–6), no fire emissions in YGP, SC, EICP, and WICP subregions, respectively. The descriptions of these six model experiments are shown in Table 2. All other emissions are included in the simulations.

4. Results

4.1. AOD Comparison Between Model and Ground-Based Observations

Table 3 shows the results of a comparison between model-simulated AOD ($0.5^\circ \times 0.667^\circ$) and CE318 Sun photometer AOD observed in each subregion and for the full study area during January 2012 to May 2013. There are 4573 matchups between Sun photometer observed and model-simulated AOD. The average value of matched Sun photometer AOD during January 2012 to May 2013 is 0.54 ± 0.45 , while the average value of matched model-simulated AOD is 0.37 ± 0.50 . Overall, the model AOD over the entire study area is moderately correlated with the ground-based AOD, with a correlation coefficient (*R*) of 0.52 (Table 3). The model

Table 3. Statistical AOD Comparisons Between CE318 Sun Photometer and Model Simulation ($0.5^\circ \times 0.667^\circ$)^a

Region	<i>N</i>	Bias	NMB	NME	RMSE	<i>R</i>	<i>y</i> Intercept	Slope
YGP	829	−0.16	−0.51	0.58	0.28	0.50	0.04	0.26
SC	413	0.00	0.01	0.41	0.34	0.57	0.00	0.70
EICP	1484	−0.18	−0.20	0.58	0.65	0.48	0.03	0.52
WICP	1847	−0.24	−0.45	0.58	0.46	0.54	0.06	0.26
Total	4573	−0.17	−0.31	0.56	0.49	0.52	0.06	0.34

^a*N* is the number of matchups. NMB represents normalized mean bias. NME is normalized mean error. RMSE stands for root-mean-square error. *R* is correlation coefficient. *y* intercept and slope stand for intercept at *y* axis and slope of the fitting line.

underestimates AOD with an average bias of −0.17. In some cases, low temporal variability (smoothness) of CE318 Sun photometer AOD within ±1.5 h caused by cloud contamination (especially in the large solar zenith angle) could lead to a positive bias of Sun photometer AOD. However, the CE318 Sun photometer AODs used here were cloud-screened, so one would expect that cloud impact was limited and not likely the major reason for the underestimation of model-simulated AOD.

Regionally, the model underestimates AOD in almost all subregions during January 2012 to May 2013. However, the model performance shows some regional dependence. The model performs best in the SC region, with virtually no bias (0.00) and the highest correlation (0.57). In the other three regions, the bias is larger than 0.16 and *R* ranges from 0.48 to 0.54. Since ground stations in WICP and SC lie in the corner of these two regions, more ground stations within the model domain are needed for better evaluation of model AOD there.

The model performance with the resolution of $0.5^\circ \times 0.667^\circ$ was also evaluated separately during March–April (the BB period) and during other months (non-BB period) (Figure 2). During these two periods, all emissions are included in the model simulations. The model AOD performs significantly better during the BB period than the non-BB period. The slope and intercept are 0.71 and 0.02, respectively, during the BB period, which contrasts with values of 0.21 and 0.07 during the non-BB period. The bias is reduced dramatically from −0.22 to −0.04, the normalized mean bias (NMB) decreased significantly from −0.50 to −0.05, the normalized mean error (NME) reduced from 0.60 to 0.51, and the correlation increases from 0.43 to 0.55 from non-BB period to BB period. These results reflect that the model performance improves when influenced by fire emissions during the BB period.

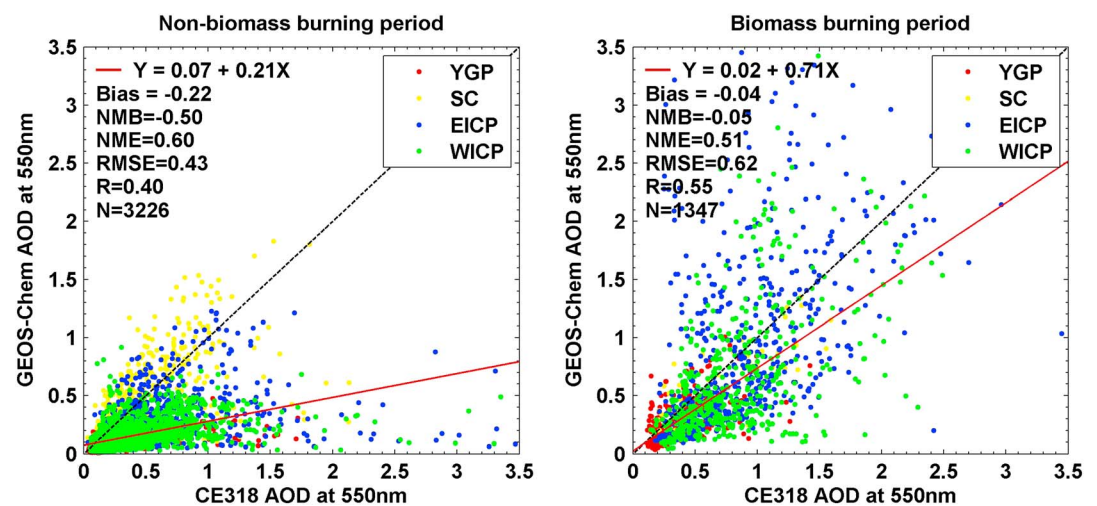


Figure 2. Comparison of AOD between CE318 Sun photometer (CE318) observation and the GEOS-Chem Exp1 simulation with the resolution of $0.5^\circ \times 0.667^\circ$ over the region $10\text{--}28^\circ\text{N}$, $90\text{--}115^\circ\text{E}$ during two time periods: (left) nonbiomass burning period (all months except for March and April) and (right) biomass burning period (March–April) during January 2012 to May 2013. Definitions of the four regions are given in Table 1 and Figure 1. The red line is the linear fitting line; the black dashed line is 1:1 line. NMB represents normalized mean bias. NME is normalized mean error. RMSE is root-mean-square error, *R* is correlation coefficient, and *N* is the number of matchups.

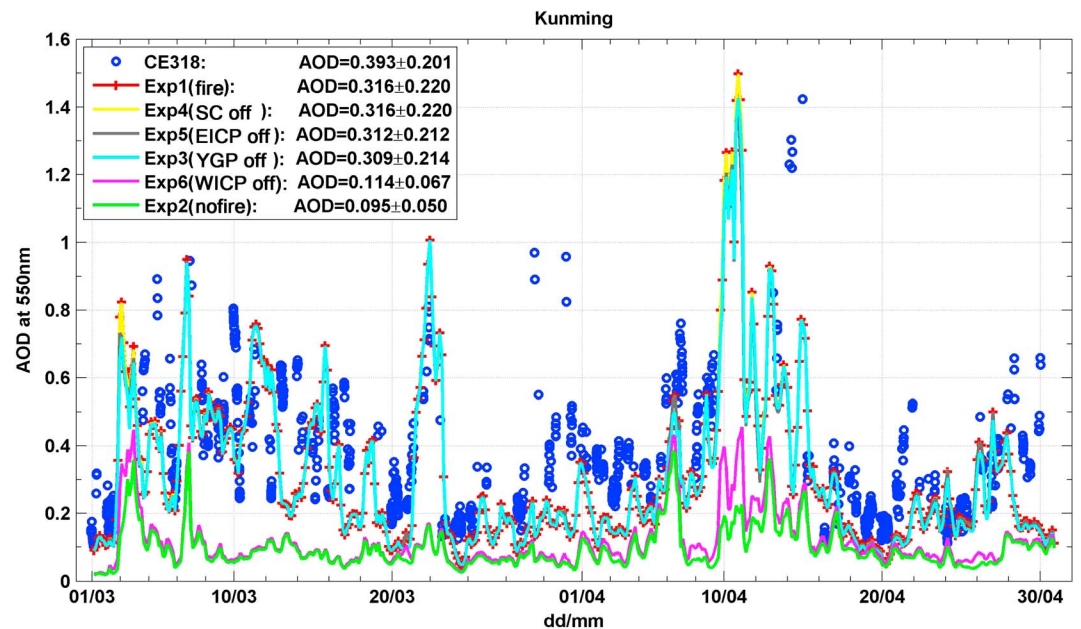


Figure 3. Time series of AOD from six GEOS-Chem simulation experiments with the resolution of $0.5^{\circ} \times 0.667^{\circ}$ (every 3 h) and CE318 Sun photometer (CE318) instantaneous observations (nominal every 15 min) at Kunming (KM) site during March–April 2013. The values in the figure (descending) are the temporal means \pm standard deviations during March–April. The values of Exp1, Exp4, Exp5, and Exp3 almost equal to each other, so some lines may be covered by the Exp3 line.

These comparisons indicate that the GEOS-Chem model still needs further improvement in AOD simulations in Southeast Asia and Southwest China, especially during the non-BB seasons. However, the model simulation with FINN emissions is able to characterize the AOD variability during the BB period, which is a sound foundation for the further analysis presented here.

We also use the ground-based Sun photometer measurements to validate the AOD simulated by the GEOS-Chem global model at $2^{\circ} \times 2.5^{\circ}$ resolution. The results show that the biases are -0.19 during January 2012 to May 2013 and -0.07 during the BB period. The biases are reduced somewhat to -0.17 and -0.04 if we use the AOD from the nested-grid model with the resolution of $0.5^{\circ} \times 0.667^{\circ}$. This indicates that model performance may be enhanced by using a finer resolution. This result agrees well with a previous study of CO transport using a finer-resolution nested-grid model [Chen *et al.* [2009].

4.2. The Influence of Smoke Transport During Biomass Burning Period

Figure 3 compares the March–April 2013 time series of instantaneous AOD from ground-based measurements (nominal every 15 min) at the KM site, located in the center of the YGP region to that simulated AOD (every 3 h) over the KM site derived from the six model experiments. The AOD at the KM site from Exp6 (no fire emission in WICP) shows a significant decrease relative to the base simulation (Exp1) and most AOD values similar between Exp6 and Exp2 (no fire emission). This indicates that the WICP region is the major contributor of BB aerosol at the KM site. The figure shows that when fire emission in other three regions is not included (Exp3–5), AOD values are close to those in Exp1, especially for Exp4 (no fire emission in SC region), suggesting that long-range transport of smoke aerosols from South China to the KM site is very rare.

In our study region where wet deposition during BB period is not significant, AOD simulated for BC and OC can be assumed to have a semilinear relationship with the emission, as in Wang *et al.* [2006]. Thus, to quantify the regional contribution of BB emissions to AOD at the KM site, four parameters are calculated. The AOD difference between Exp1 and Exp2 reflects the potential contribution of total BB (referred to as BB_AOD_{total}) at the KM site. The AOD differences between Exp1 and Exp3–6 reflect the corresponding contribution of BB AOD from each region (referred to as BB_AOD_{region}) at the KM site. Therefore, BB_AOD_{region} divided by BB_AOD_{total} is the ratio of regional BB AOD to total BB AOD (referred to as $ratio_{BB_AOD}$), and BB_AOD_{region}

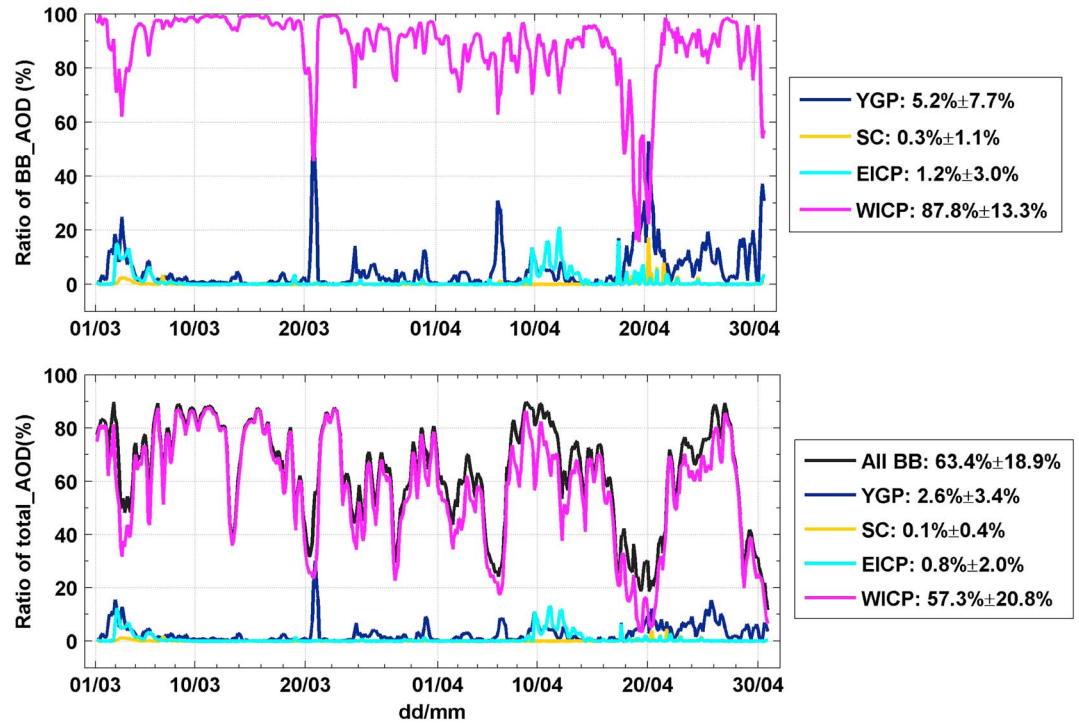


Figure 4. Time series of the contribution ratios of biomass burning in four regions to (top) biomass burning AOD and to (bottom) total AOD over Kunming during March–April 2013. The four regions are Yungui Plateau (YGP), South China (SC), East of Indochinese Peninsula (EICP), and West of Indochinese Peninsula (WICP). “All BB” stands for the contribution of all biomass burning aerosol to the total AOD at KM site.

divided by the AOD from Exp1 represents the ratio of regional BB AOD to total AOD (referred to as $ratio_{total_AOD}$) at the KM site. These parameters are calculated as follows:

$$BB_AOD_{total} = AOD_{Exp1} - AOD_{Exp2} \tag{1}$$

$$BB_AOD_{region_n} = AOD_{Exp1} - AOD_{Expn}, \quad (n = 3, 4, 5, 6) \tag{2}$$

$$ratio_{BB_AOD}(region_n) = \frac{BB_AOD_{region_n}}{BB_AOD_{total}} \tag{3}$$

$$ratio_{total_AOD}(region_n) = \frac{BB_AOD_{region_n}}{AOD_{Exp1}} \tag{4}$$

where n is 3, 4, 5, and 6, representing the region of YGP, SC, EICP, and WICP, respectively. Assume that Exp2–6 have the same error as Exp1 and each experiment is independent, the errors of $ratio_{BB_AOD}$ and $ratio_{total_AOD}$ are 2 times and 1.73 times larger than the error of Exp1 according to the propagation of error, respectively.

The quantitative estimates of regional contributions of smoke aerosols to AOD at the KM site are shown in Figure 4. The regional values of temporal average and standard deviation of $ratio_{BB_AOD}$ are $5.2\% \pm 7.7\%$, $0.3\% \pm 1.1\%$, $1.2\% \pm 3.0\%$, and $87.8\% \pm 13.3\%$, and the values of $ratio_{total_AOD}$ are $2.6\% \pm 3.4\%$, $0.1\% \pm 0.4\%$, $0.8\% \pm 2.0\%$, and $57.3\% \pm 20.8\%$ for the YGP, SC, EICP, and WICP regions, respectively. These results suggest that long-range transport of BB aerosols from WICP region to Southwest China significantly impacts the aerosol loading at the KM site. The contribution of local (YGP region) BB pollution to AOD at KM is marginal, followed by BB in the EICP region. The transport from the SC region is nearly negligible. Notably, the sum of the regional $ratio_{BB_AOD}$ from the four regions is 94.5%, which suggests that the KM site may be affected by long-range smoke transport from other region, such as India. Figure 4 shows that the WICP region is largest contributor to both BB_AOD and $total_AOD$ during the most of BB period. There is a couple days when local pollution (YGP region) is dominant, such as the end of 20 March and all day on 20 April. The contribution of all BB

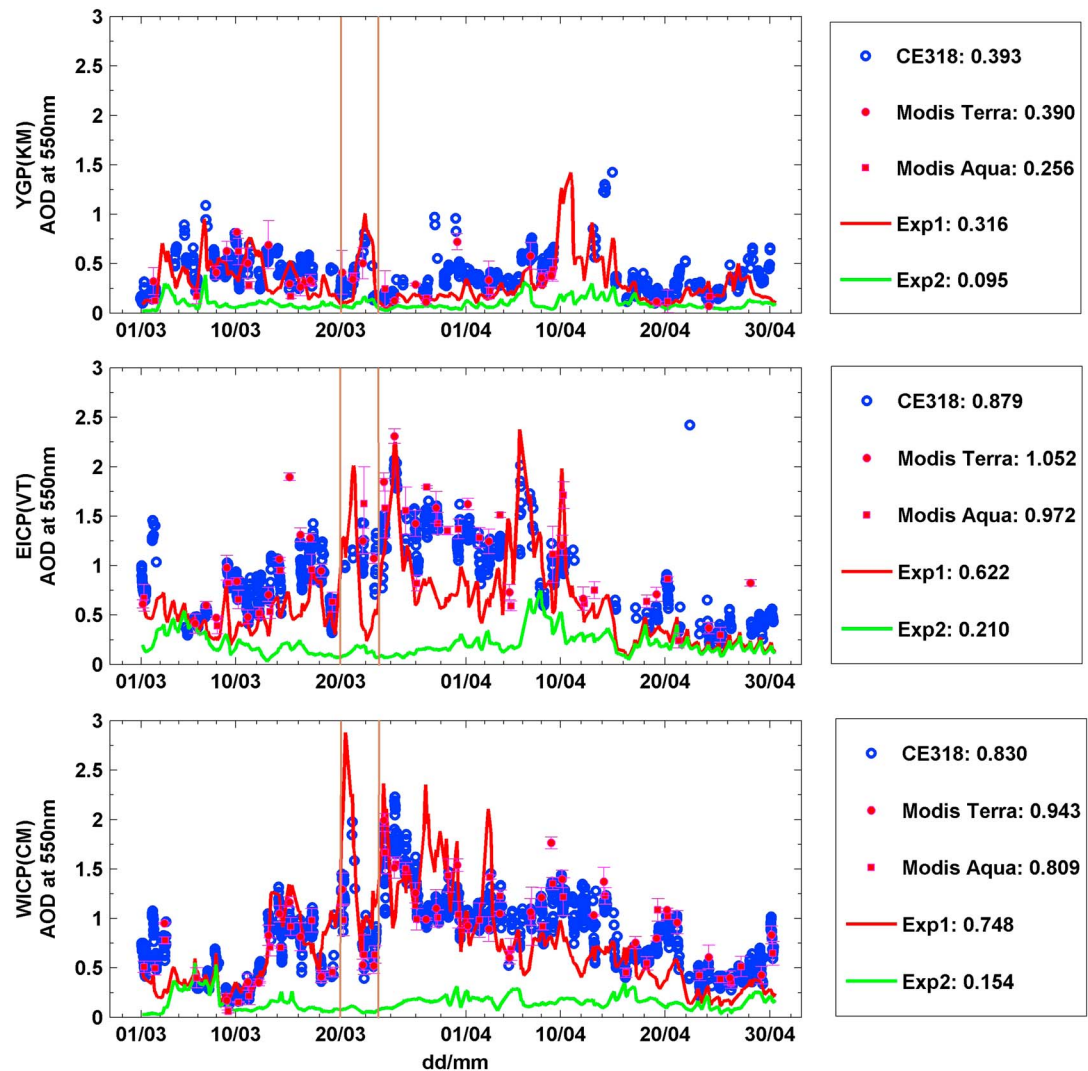


Figure 5. March–April 2013 time series of AOD at 550 nm over three sites: KM (YGP region), VT (EICP region), and CM (WICP region). The blue circles indicate CE318 Sun photometer observed AOD; the pink dots and squares indicate MODIS AOD from Terra and Aqua, respectively; the red line indicates GEOS-Chem simulated AOD ($0.5^\circ \times 0.667^\circ$) with fire emission (Exp1); and the green line indicates model AOD ($0.5^\circ \times 0.667^\circ$) without fire emission (Exp2). The MODIS AOD values and their error bars are reported as the mean \pm standard deviation of 3×3 MODIS AOD retrievals (at 10 km resolution) centered at the CE318 Sun photometer site. The values in the legend are the averages over the time period.

aerosol to total AOD at KM (i.e., the sum of regional $\text{ratio}_{\text{total_AOD}}$) is $63.4\% \pm 18.9\%$ during March–April 2013 (Figure 4, bottom), which indicates that other aerosol types are also present in Southwest China.

The uncertainty of these ratios should depend on AOD simulations that can affect by the uncertainty in aerosol source inventories (fire emission inventory and other aerosol emission inventories). *Wiedinmyer et al.* [2011] assigned that the uncertainty of FINN is approximately a factor of 2, although *Zhang et al.* [2014] showed that FINN estimate is in the middle-to-low range of fire emission estimates by different groups. Hence, the low bias of AOD in our simulation is most likely due to underestimation of both fire and anthropogenic emissions. Furthermore, our sensitivity simulations similar as Exp1 and Exp6 with an 50% variation of FINN show that the $\text{ratio}_{\text{BB_AOD}}$ and $\text{ratio}_{\text{total_AOD}}$ for WICP region are $85.8\% \pm 18.5\%$ and $43.9\% \pm 20.0\%$, respectively. Comparing to the results of simulations with baseline FINN, the value of $\text{ratio}_{\text{BB_AOD}}$ shows a small variation (from 87.8% to 85.8%), while $\text{ratio}_{\text{total_AOD}}$ shows relatively larger variation (from 57.3% to 43.9%), which indicates that the biomass burning aerosols are the major aerosol type and regulate the AOD variation in WICP region, which is consistent from our past analysis based on the Sun

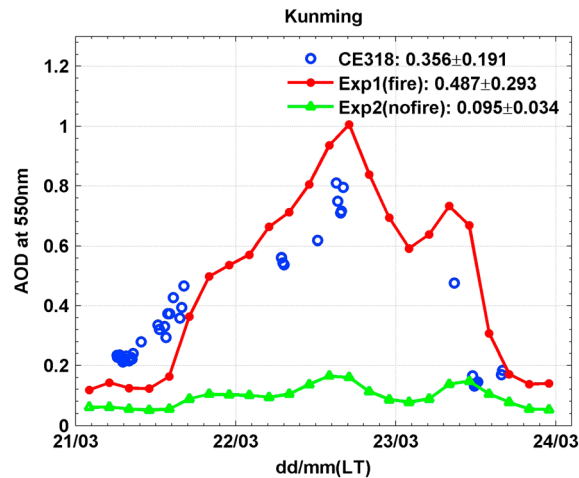


Figure 6. CE318 Sun photometer (CE318) observed and model simulated AOD with the resolution of $0.5^\circ \times 0.667^\circ$ at Kunming during 21–23 March 2013. The red line is the model simulation including global fire emission (Exp1), and the green line is the model simulation with no fire emission (Exp2). LT is the local time (LT = UTC + 8 h).

4.3. A Case Study of Westerly Smoke Transport to KM

A specific case of long-range transport of BB aerosols to the KM site is analyzed further. This case is selected based on a combination of observations and model simulations. Figure 5 shows the time series of observed (CE318 Sun photometer and MODIS) and simulated AOD (Exp1 and Exp2) at the KM (YGP region), VT (EICP region), and CM (WICP region) sites during March–April 2013. Each site represents a corresponding subregion. The SC region is not included in this analysis since there are few ground observations during this period. The MODIS AOD is mostly consistent with the CE318 AOD. Further, the model simulation including FINN emissions (Exp1) captures the changing trends in observed AOD, especially during AOD peaks, such as 22 March at the KM site, 25 March and 7 April at the VT site, and 20 March at the CM site. Notably, the three sites all show peak values of AOD during 20–23 March and the peak at KM site occurs later than at the other two sites. In addition, Figure 4 (top) shows that the contribution of BB from WICP to AOD at the KM site decreases to 40%–70% from 15:00 UTC 20 March to 03:00 UTC 21 March but rapidly increases to 90% after 06:00 UTC on 21 March, which indicates smoke transport from WICP to the KM site after 06:00 UTC 21 March. Therefore, this time period of elevated aerosol loading (21–23 March) is investigated further.

Time series of AOD at the KM site derived from CE318 Sun photometer and the GEOS-Chem model simulations during 21–23 March 2013 are shown in Figure 6. The mean values of AOD from CE318 Sun photometer and Exp1 are respectively 0.36 and 0.49, both of which are much higher than that calculated from Exp2 (0.10), suggesting that BB aerosol is the dominant aerosol type during this time period. On 21 March, the AOD derived from the Sun photometer increases from 0.21 in the morning to 0.48 in the afternoon. Similar increases in AOD are also simulated by the model Exp1 (from 0.12 at 02:00 A.M. to 0.54 at 23:00 P.M. LT). This increase of AOD continues to 22 March. The Sun photometer AOD increases from 0.55 at 07:00 to 0.80 at 16:00 LT, which is captured by the model Exp1 simulation. The model Exp1 AOD decreases after 17:00 LT when Sun photometer measurements are not available. On 23 March, the Sun photometer AOD dramatically decreases from 0.48 at 09:00 to 0.18 at 16:00 LT. The model Exp1 AOD on 23 March shows a slight increase during 02:00 to 08:00 LT but decreases from 08:00 LT to the end of this day. Overall, AOD variation from the model simulation (Exp1) is in good agreement with that measured by the Sun photometer during these three days.

Figure 7 presents the MODIS true-color images overlaid by MODIS active fire location (first row), MODIS and model Exp1 AOD distributions (second and third row), and synoptic meteorology (last row) during 21–23 March 2013. The greatest fire activity is observed on 22 March. The regions with high MODIS AODs (Figure 7, second row) correspond well to the thick smoke layer in northern EICP (Laos and Vietnam) and WICP (north east India and Burma). A large area of high MODIS AOD is shown in north Burma on 21–22 March. Coincidentally, these two days are shown with the increased AOD observed by ground observation at the KM site (Figure 6).

photometer data and back trajectory analysis [Zhu *et al.*, 2016]. This conclusion is not consistent with Zhang *et al.* [2012] showing that mineral dust is a major (and sometimes dominant) type in China. This inconsistency in part is due to the sampling locations; the closest sampling location in Zhang *et al.* [2012] is ~800 km northwest from KM and thereby is much closer to the Asian dust source region. The inconsistency can also be caused by the difference in measurement techniques and the time periods; Cao *et al.* [2012] and Xin *et al.* [2015] showed that sulfate and organic matter shared a far greater contribution to aerosol mass in various Chinese cities [Cao *et al.*, 2012; Xin *et al.*, 2015]. Therefore, we conclude that the BB aerosol has a dominant influence over KM site in the Spring season (about 63% contribution to total AOD at KM simulated by FINN during March–April 2013).

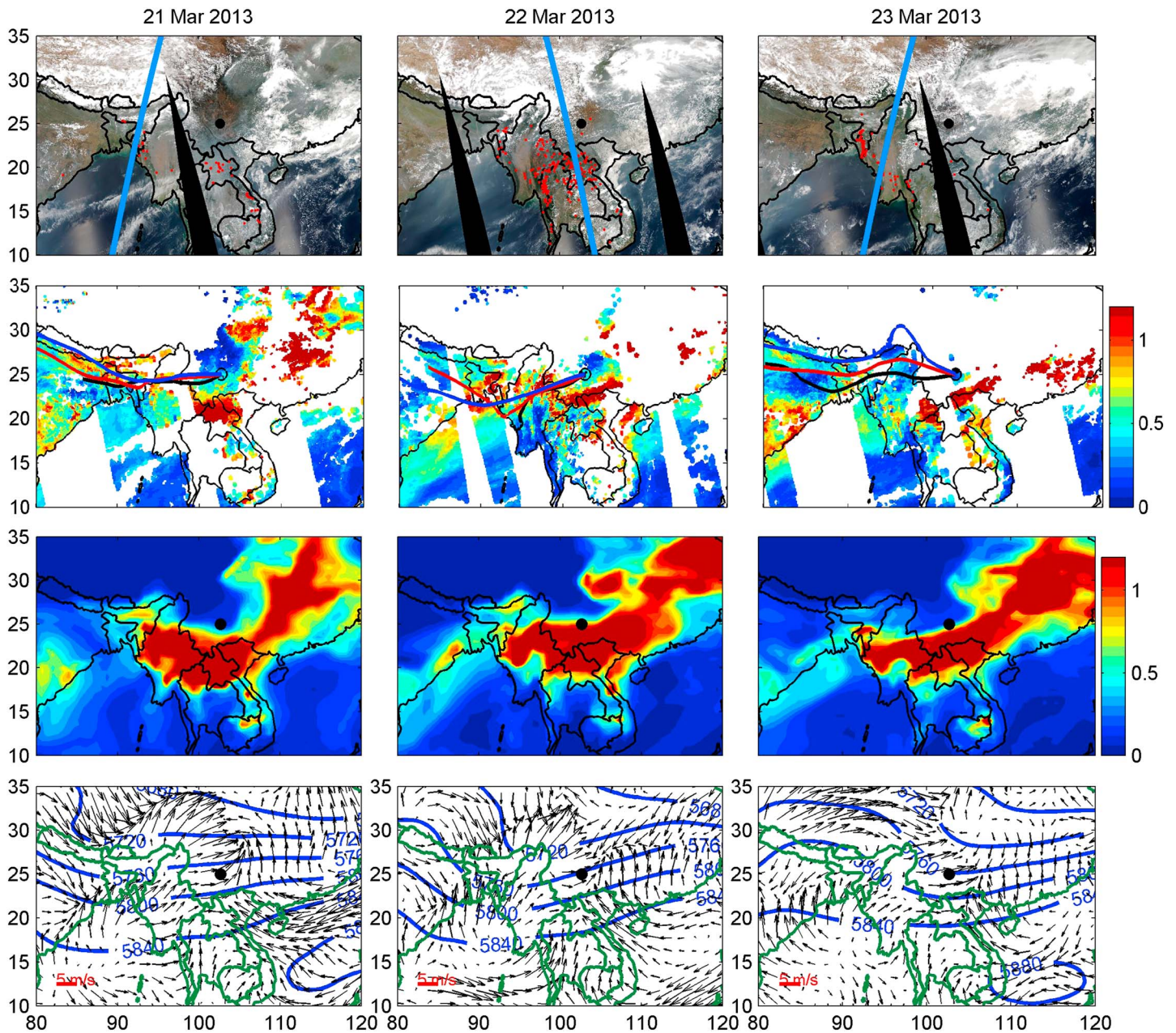


Figure 7. (first row) MODIS true color images overlaid by fire points, (second row) MODIS AOD and 72 h back trajectories at Kunming, (third row) model Exp1 AOD with the resolution of $0.5^\circ \times 0.667^\circ$, and (last row) NCEP daily surface wind (m/s) and 500 Mb geopotential height (m) over the region of $80\text{--}120^\circ\text{E}$ and $10\text{--}35^\circ\text{N}$ on 21–23 March 2013. The black dot shows the location of Kunming site (KM). In the first row, the blue lines are the ground track of CALIPSO satellite and the red dots are MODIS active fire locations on the day. The three back trajectories on each day in the second row are black for 2000 m, red for 3000 m, and blue for 4000 m agl.

The model Exp1 AOD (Figure 7, third row) also shows the smoke transport from west to east. The KM site (black circle in the figure) is closest to the area with high modeled AOD on 22 March when the largest AOD is observed by CE318 Sun photometer there. The centers of the areas with elevated modeled AOD correspond well with those of MODIS AOD, but the modeled areas with elevated AOD (where $\text{AOD} > 1.0$) are larger than those observed by MODIS (Figure 7, second row). Both the MODIS and model Exp1 AOD over northern Laos and Vietnam are very high, and these elevated values extend to South China, illustrating the transport of smoke from Southeast Asia to South China such as Guangzhou [Deng et al., 2008] and Hong Kong [Chan et al., 2003]. However, the smoke transport to YGP is mostly related to BB in Burma and Northeast India, which is supported by the following analysis.

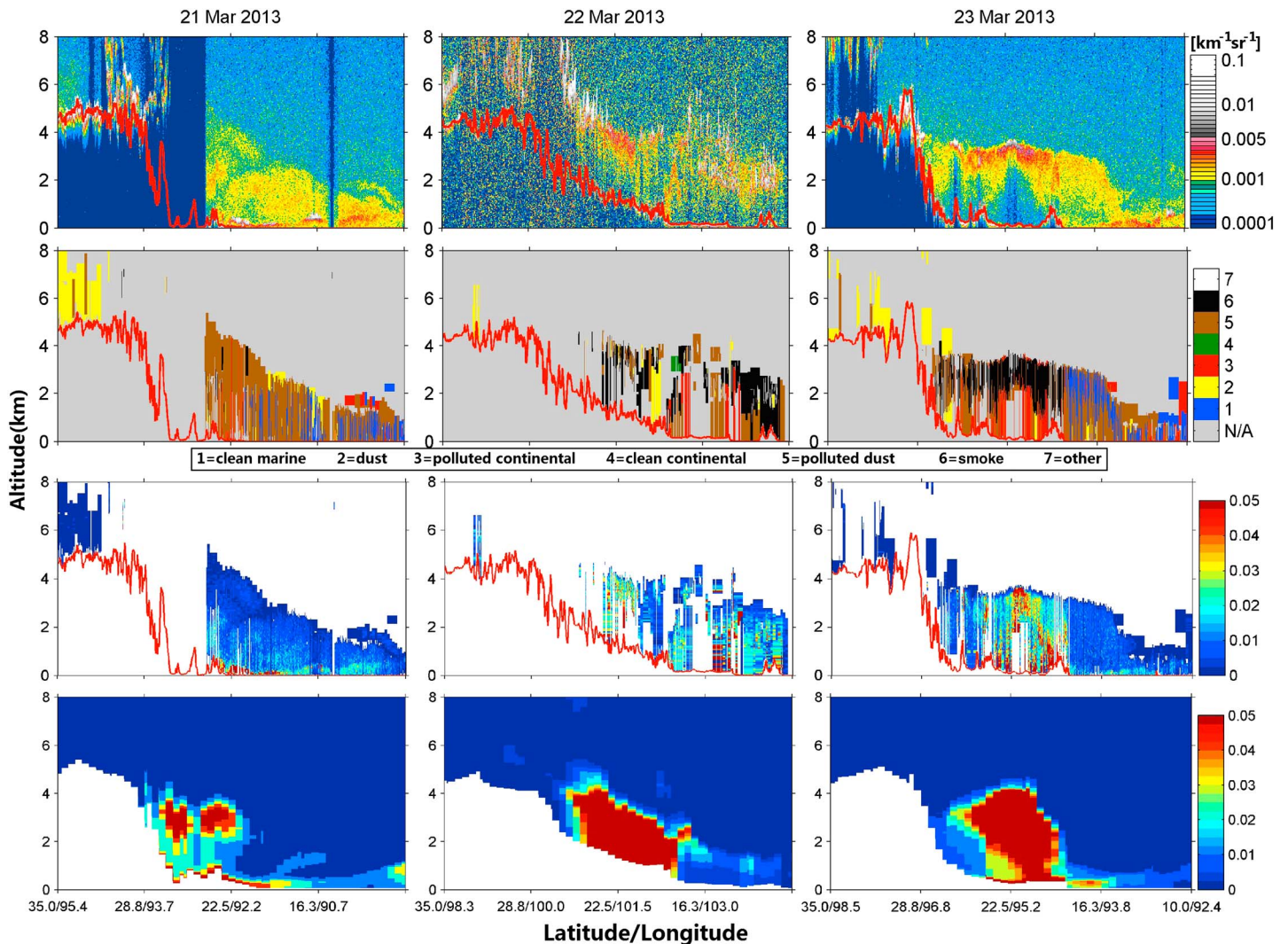


Figure 8. (first row) 21–23 March 2013 CALIOP-derived vertical profile of total attenuated backscatter at 532 nm, (second row) vertical feature mask of aerosol, and (third row) vertical AOD at 532 nm (multiple particle extinction coefficient by the level thickness) over the ground track shown in Figure 7 first row, along with the GEOS-Chem ($0.5^\circ \times 0.667^\circ$) Exp1 simulated vertical profiles of total AOD at 550 nm along the corresponding (last row) CALIPSO ground track and overpass time. The red lines are the surface height from the CALIPSO satellite.

Analysis of the synoptic patterns during this time period (Figure 7, bottom row) shows that the majority of the WICP region (mainly northeast India and Burma) is located in the front of a trough during 21–22 March. More importantly, surface winds show a convergence in northern Burma ($23\text{--}25^\circ\text{N}$, $90\text{--}100^\circ\text{E}$), which is favorable for the uplift of smoke aerosols to higher altitudes. As a result of the westerly and southwesterly winds at the middle troposphere over this region, BB aerosols are eventually transported to the YGP. With the easterly movement of the trough from 21 March to 23 March, the WICP region is then located behind the trough on 23 March, which is unfavorable for the uplift of smoke aerosol in this region. Furthermore, airflow over the KM site is from the northwest (i.e., air masses are from the Tibetan Plateau) on 23 March and afterward (this can also be deduced by the back trajectory at 4000 m agl on 23 March in Figure 7, second row). This synoptic change prevents long-range transport of BB aerosols from the WICP region to the YGP. On the contrary, clean air masses transported from Tibetan Plateau lead to a decrease of AOD on 23 March. Notably, although there is a convergence and updraft in north Laos and Vietnam (in the EICP region), the westerly wind overhead prevents transport of BB aerosols from the EICP region to the YGP. The synoptic patterns, combining the AOD variations on the three days, indicate that smoke aerosols take 1 day or less to transport from Northeast India and Burma to the KM site.

The potential for long-range transport of the uplifted WICP smoke aerosol depends on the altitude to which the aerosol is lifted. Figure 8 shows the vertical profile of aerosols derived from the CALIOP satellite measurements and the model simulation. We choose the nearest CALIPSO ground track to the west of the KM site (locations shown in Figure 7, first row) to identify the largest contribution of smoke from the WICP region. Due to the high-surface height and clouds, the aerosol layer in the north of ground track is not obvious. During 21–23 March, the level 1 attenuated backscatter at 532 nm derived from CALIOP shows apparent aerosol layers between the surface and 5 km (Figure 8, first row). The AOD profile from CALIOP (using the CALIOP AOD profile instead of particle extinction coefficient is to compare with GEOS-Chem simulated AOD) shown in the third row shows different patterns of aerosol profiles on the three days: high values near the surface on 21 March but rising to about 4 km on 22–23 March over the latitude of $\sim 22^\circ\text{N}$. Furthermore, the aerosol type corresponding to high values of CALIOP AOD on 22–23 March is mostly attributable to smoke aerosol according to the CALIOP vertical profile of aerosol subtype (Figure 8, second row, black points). These CALIOP observations support the idea of smoke aerosol transport from low-altitude sources west of the YGP (Northeast India and Burma) to the 2 km altitude of the KM site. Compared to the CALIOP observations, the plume height (4–5 km) and vertical profile of AOD simulated by the model (Figure 8, last row) are in good agreement with the CALIOP observations on 22–23 March, especially for the track between ~ 19 and 27°N . Therefore, the full story of long-range transport of BB from Northeast India and Burma to the YGP as revealed by a combination of observations and model simulations is as follows: smoke aerosols accumulate as a result of BB in Northeast India and Burma; smoke aerosols are pumped into higher level of the atmosphere (4–5 km); and BB aerosols are transported to the YGP via the prevailing westerly wind.

5. Conclusions

We have simulated the spatial-temporal variation of AOD by using the GEOS-Chem nested-grid model with FINN BB emissions and other anthropogenic emissions over Southeast Asia. The model performance was evaluated by comparing model AOD against ground-based Sun photometer data at eight stations. Long-range transport of BB aerosols from surrounding regions to the KM site, a station located in the YGP region in southwest China, was quantitatively evaluated. The main conclusions are as follows:

1. The GEOS-Chem nested-grid model simulation with a spatial resolution of $0.5^\circ \times 0.667^\circ$ underestimates the AOD value by 0.17 during January 2012 to May 2013. The model performs much better in BB months (March–April), with an AOD bias only of -0.04 . The temporal variation of AOD in BB months is well captured by the model, with a correlation coefficient of 0.55. The performance of GEOS-Chem simulation of AOD apparently needs further improvement, especially during nonburning period.
2. BB in Northeast India and Burma is the largest contributor of BB AOD and total AOD at the KM site during BB months (March–April). Long-range transport of smoke aerosol from these areas accounts for about 88% of the calculated BB AOD and about 57% of total AOD at the KM site. This large contribution is persistent throughout nearly the entire BB period.
3. The modeled spatial distribution of AOD and vertical profile of aerosols are consistent with their respective counterparts derived from MODIS and CALIOP measurements. Layers of BB aerosol can reach 4 km altitude in the western part of the YGP. The prevailing westerly airflow and the larger amount of smoke emitted in Northeast India and Burma lead to the possibility of long-range transport of smoke from these regions to the YGP region.

Finally, we note that quantitative impact of BB transport from Southeast Asia to YGP largely depends on the inventories of smoke emissions that can vary year by year. Furthermore, the underestimation of simulated AOD in the months without biomass burning is unclear, although it is likely that the seasonal variation of industrial emissions may not be well represented in the model [Wang *et al.*, 2016]. Therefore, further studies of smoke transport in other years as well as long-term observation of aerosol properties (especially from accurate ground-based measurements) are required to quantify both the impacts of biomass burning aerosols and anthropometric aerosols on the air quality and climate in this region.

Acknowledgments

This work is supported by the National Science Foundation of China (41475138), the Strategic Priority Research Program of the Chinese Academy of Sciences (XDA05100301), and the Startup Fund for Talent of Nanjing University of Information Science and Technology. The authors thank the PI investigators (Janet Elizabeth Nichol, Brent Holben, Serm Janjai, and Nguyen Xuan Anh) and their staff for establishing and maintaining the sites (HK, ZU, VT, LN, ND, CM, and DU) used in this investigation. The authors are also grateful to the group members of Jun Wang. J.A.F. acknowledges support from a University of Wollongong Vice Chancellor's Fellowship and the assistance of resources provided at the NCI National Facility systems at the Australian National University through the National Computational Merit Allocation Scheme supported by the Australian government. AERONET data are downloaded from the website of <http://aeronet.gsfc.nasa.gov>. The Sun photometer data of Kunming site used in this paper can be obtained from the first author (J. Zhu) through e-mail (junzhu@nuist.edu.cn). The MODIS aerosol and active fire products are available from the Atmosphere Archive and Distribution System (LAADS) website (<http://ladsweb.nascom.nasa.gov>) and the University of Maryland website (<ftp://fuoco.geog.umd.edu>), respectively. The CALIPSO data are from the Atmospheric Science Data Center (ASDC) website (<https://eosweb.larc.nasa.gov>). NCEP/NCAR Reanalysis data are downloaded from the Earth System Research Laboratory website (<http://www.esrl.noaa.gov>). The HEMCO emission data used in GEOS-Chem model can refer to GEOS-Chem Wiki website (http://wiki.seas.harvard.edu/geos-chem/index.php/Main_Page). All modeling results presented in this manuscript can be obtained upon request to J. Wang, jun-wang-1@uiowa.edu.

References

- Akagi, S. K., R. J. Yokelson, C. Wiedinmyer, M. J. Alvarado, J. S. Reid, T. Karl, J. D. Crouse, and P. O. Wennberg (2011), Emission factors for open and domestic biomass burning for use in atmospheric models, *Atmos. Chem. Phys.*, *11*(9), 4039–4072.
- Ångström, A. (1929), On the atmospheric transmission of Sun radiation and on dust in the air, *Geogr. Ann.*, *11*, 156–166.
- Ansmann, A., H. Baars, M. Tesche, D. Müller, D. Althausen, R. Engelmann, T. Pauliquevis, and P. Artaxo (2009), Dust and smoke transport from Africa to South America: Lidar profiling over Cape Verde and the Amazon rainforest, *Geophys Res Lett*, *36*, L11802, doi:10.1029/2009GL037923.
- Aouizerats, B., G. R. van der Werf, R. Balasubramanian, and R. Betha (2015), Importance of transboundary transport of biomass burning emissions to regional air quality in Southeast Asia, *Atmos. Chem. Phys.*, *15*(1), 363–373.
- Bey, I., D. J. Jacob, R. M. Yantosca, J. A. Logan, B. D. Field, A. M. Fiore, Q. B. Li, H. G. Y. Liu, L. J. Mickley, and M. G. Schultz (2001), Global modeling of tropospheric chemistry with assimilated meteorology: Model description and evaluation, *J. Geophys. Res.*, *106*, 23,073–23,095, doi:10.1029/2001JD000807.
- Bond, T. C., D. G. Streets, K. F. Yarber, S. M. Nelson, J. H. Woo, and Z. Klimont (2004), A technology-based global inventory of black and organic carbon emissions from combustion, *J. Geophys. Res.*, *109*, D14203, doi:10.1029/2003JD003697.
- Bond, T. C., E. Bhardwaj, R. Dong, R. Jogani, S. K. Jung, C. Roden, D. G. Streets, and N. M. Trautmann (2007), Historical emissions of black and organic carbon aerosol from energy-related combustion, 1850–2000, *Global Biogeochem. Cycles*, *21*, GB2018, doi:10.1029/2006GB002840.
- Cao, J. J., Z. X. Shen, J. C. Chow, J. G. Watson, S. C. Lee, X. X. Tie, and Y. M. Han (2012), Winter and summer PM_{2.5} chemical compositions in fourteen Chinese cities, *J. Air Waste Manage.*, *62*(10), 1214–1226, doi:10.1080/10962247.2012.701193.
- Chan, C. Y., L. Y. Chan, J. M. Harris, S. J. Oltmans, D. R. Blake, Y. Qin, Y. G. Zheng, and X. D. Zheng (2003), Characteristics of biomass burning emission sources, transport, and chemical speciation in enhanced springtime tropospheric ozone profile over Hong Kong, *J. Geophys. Res.*, *108*(D1), 4015, doi:10.1029/2001JD001555.
- Chen, D., Y. Wang, M. B. McElroy, K. He, R. M. Yantosca, and P. Le Sager (2009), Regional CO pollution and export in China simulated by the high-resolution nested-grid GEOS-Chem model, *Atmos. Chem. Phys.*, *9*(11), 3825–3839.
- Crutzen, P. J., and M. O. Andreae (1990), Biomass burning in the tropics—Impact on atmospheric chemistry and biogeochemical cycles, *Science*, *250*(4988), 1669–1678.
- Damoah, R., N. Spichtinger, C. Forster, P. James, I. Mattis, U. Wandinger, S. Beirle, T. Wagner, and A. Stohl (2004), Around the world in 17 days—Hemispheric-scale transport of forest fire smoke from Russia in May 2003, *Atmos. Chem. Phys.*, *4*(5), 1311–1321.
- Deng, X., X. Tie, X. Zhou, D. Wu, L. Zhong, H. Tan, F. Li, X. Huang, X. Bi, and T. Deng (2008), Effects of Southeast Asia biomass burning on aerosols and ozone concentrations over the Pearl River Delta (PRD) region, *Atmos. Environ.*, *42*(36), 8493–8501.
- Draxler, R. R., and G. D. Hess (1998), An overview of the HYSPLIT-4 Modelling system for trajectories, dispersion and deposition, *Austr. Meteorol. Mag.*, *47*, 295–308.
- Drury, E., D. J. Jacob, J. Wang, R. J. D. Spurr, and K. Chance (2008), Improved algorithm for MODIS satellite retrievals of aerosol optical depths over western North America, *J. Geophys. Res.*, *113*, D16204, doi:10.1029/2007JD009573.
- Eck, T. F., B. N. Holben, J. S. Reid, O. Dubovik, A. Smirnov, N. T. O'Neill, I. Slutsker, and S. Kinne (1999), Wavelength dependence of the optical depth of biomass burning, urban, and desert dust aerosols, *J. Geophys. Res.*, *104*, 31,333–31,349, doi:10.1029/1999JD00923.
- Engling, G., and A. Gelencser (2010), Atmospheric brown clouds: From local air pollution to climate change, *Elements*, *6*(4), 223–228.
- Engling, G., Y. N. Zhang, C. Y. Chan, X. F. Sang, M. Lin, K. F. Ho, Y. S. Li, C. Y. Lin, and J. J. Lee (2011), Characterization and sources of aerosol particles over the southeastern Tibetan Plateau during the Southeast Asia biomass-burning season, *Tellus B*, *63*(1), 117–128.
- Engling, G., J. He, R. Betha, and R. Balasubramanian (2014), Assessing the regional impact of Indonesian biomass burning emissions based on organic molecular tracers and chemical mass balance modeling, *Atmos. Chem. Phys.*, *14*(14), 8043–8054.
- European Commission, Joint Research Centre (JRC)/Netherlands Environmental Assessment Agency (PBL) (2009), Emission Database for Global Atmospheric Research (EDGAR), release version 4.0. [Available at <http://edgar.jrc.ec.europa.eu>]
- Fairlie, T. D., D. J. Jacob, and R. J. Park (2007), The impact of transpacific transport of mineral dust in the United States, *Atmos. Environ.*, *41*(6), 1251–1266.
- Fisher, J. A., et al. (2011), Sources, distribution, and acidity of sulfate-ammonium aerosol in the Arctic in winter-spring, *Atmos. Environ.*, *45*(39), 7301–7318.
- Holben, B. N., et al. (1998), AERONET a federated instrument network and data archive for aerosol characterization, *Remote Sens. Environ.*, *66*, 1–16.
- Hu, L., D. B. Millet, M. Baasandorj, T. J. Griffis, K. R. Travis, C. W. Tessum, J. D. Marshall, W. F. Reinhart, T. Mikoviny, and M. Müller (2015), Emissions of C₆–C₈ aromatic compounds in the United States: Constraints from tall tower and aircraft measurements, *J. Geophys. Res.*, *120*, 826–842, doi:10.1002/2014JD022627.
- Huang, K., J. S. Fu, N. C. Hsu, Y. Gao, X. Dong, S.-C. Tsay, and Y. F. Lam (2013), Impact assessment of biomass burning on air quality in Southeast and East Asia during BASE-ASIA, *Atmos. Environ.*, *78*, 291–302.
- International Panel on Climate Change (2013), *Climate Change 2013: The Physical Science Basis. Contribution of Working Group I to the Fifth Assessment Report of the Intergovernmental Panel on Climate Change*, 1535 pp., Cambridge Univ. Press, Cambridge, U. K., and New York.
- Jacob, D. J., J. H. Crawford, M. M. Kleb, V. S. Connors, R. J. Bendura, J. L. Raper, G. W. Sachse, J. C. Gille, L. Emmons, and C. L. Heald (2003), Transport and Chemical Evolution over the Pacific (TRACE-P) aircraft mission: Design, execution, and first results, *J. Geophys. Res.*, *108*(D20), 9000, doi:10.1029/2002JD003276.
- Jacobson, M. Z. (2001), Strong radiative heating due to the mixing state of black carbon in atmospheric aerosols, *Nature*, *409*(6821), 695–697.
- Jaffe, D., I. Bertschi, L. Jaegle, P. Novelli, J. S. Reid, H. Tanimoto, R. Vingarzan, and D. L. Westphal (2004), Long-range transport of Siberian biomass burning emissions and impact on surface ozone in western North America, *Geophys. Res. Lett.*, *31*, L16106, doi:10.1029/2004GL020093.
- Kalnay, E., et al. (1996), The NCEP/NCAR 40-year reanalysis project, *Bull. Am. Meteorol. Soc.*, *77*(3), 437–471.
- Keller, C. A., M. S. Long, R. M. Yantosca, A. M. Da Silva, S. Pawson, and D. J. Jacob (2014), HEMCO v1.0: A versatile, ESMF-compliant component for calculating emissions in atmospheric models, *Geosci. Model Dev. Discuss.*, *7*(1), 1115–1136.
- Lee, C., R. V. Martin, A. van Donkelaar, H. Lee, R. R. Dickerson, J. C. Hains, N. Krotkov, A. Richter, K. Vinnikov, and J. J. Schwab (2011), SO₂ emissions and lifetimes: Estimates from inverse modeling using in situ and global, space-based (SCIAMACHY and OMI) observations, *J. Geophys. Res.*, *116*, D06304, doi:10.1029/2010JD014758.
- Leibensperger, E. M., L. J. Mickley, D. J. Jacob, W. T. Chen, J. H. Seinfeld, A. Nenes, P. J. Adams, D. G. Streets, N. Kumar, and D. Rind (2012), Climatic effects of 1950–2050 changes in US anthropogenic aerosols—Part 1: Aerosol trends and radiative forcing, *Atmos. Chem. Phys.*, *12*(7), 3333–3348.

- Levy, R. C., S. Mattoo, L. A. Munchak, L. A. Remer, A. M. Sayer, and N. C. Hsu (2013), The Collection 6 MODIS aerosol products over land and ocean, *Atmos. Meas. Tech. Discuss.*, *6*(1), 159–259.
- Lin, C.-Y., C. Zhao, X. Liu, N.-H. Lin, and W.-N. Chen (2014), Modelling of long-range transport of Southeast Asia biomass-burning aerosols to Taiwan and their radiative forcings over East Asia, *Tellus Ser. B, Chem. Phys. Meteorol.*, *66*, 23,733, doi:10.3402/tellusb.v66.23733.
- Lin, J. T., and M. B. McElroy (2010), Impacts of boundary layer mixing on pollutant vertical profiles in the lower troposphere: Implications to satellite remote sensing, *Atmos. Environ.*, *44*(14), 1726–1739.
- Lin, S. J., and R. B. Rood (1996), Multidimensional flux-form semi-Lagrangian transport schemes, *Mon. Weather Rev.*, *124*(9), 2046–2070.
- Liu, H., D. J. Jacob, I. Bey, and R. M. Yantosca (2001), Constraints from ²¹⁰Pb and ⁷Be on wet deposition and transport in a global three-dimensional chemical tracer model driven by assimilated meteorological fields, *J. Geophys. Res.*, *106*, 12,109–12,128, doi:10.1029/2000JD900839.
- Liu, J. H., J. A. Logan, D. B. A. Jones, N. J. Livesey, I. Megretskaia, C. Carouge, and P. Nedelec (2010), Analysis of CO in the tropical troposphere using Aura satellite data and the GEOS-Chem model: Insights into transport characteristics of the GEOS meteorological products, *Atmos. Chem. Phys.*, *10*(24), 12,207–12,232.
- Menon, S., J. Hansen, L. Nazarenko, and Y. Luo (2002), Climate effects of black carbon aerosols in China and India, *Science*, *297*(5590), 2250–2253.
- Mielonen, T., H. Portin, M. Komppula, A. Leskinen, J. Tamminen, I. Jalongo, J. Hakkarainen, K. E. J. Lehtinen, and A. Arola (2012), Biomass burning aerosols observed in Eastern Finland during the Russian wildfires in summer 2010—Part 2: Remote sensing, *Atmos. Environ.*, *47*, 279–287.
- Olivier, J. G. J., J. A. Van Aardenne, F. J. Dentener, V. Pagliari, L. N. Ganzeveld, and J. A. H. W. Peters (2005), Recent trends in global greenhouse gas emissions: Regional trends 1970–2000 and spatial distribution of key sources in 2000, *Environ. Sci.*, *2*(2–3), 81–99.
- Penner, J. E., R. E. Dickinson, and C. A. Oneill (1992), Effects of aerosol from biomass burning on the global radiation budget, *Science*, *256*(5062), 1432–1434.
- Peppler, R. A., et al. (2000), ARM Southern Great Plains site observations of the smoke pall associated with the 1998 Central American fires, *Bull. Am. Meteorol. Soc.*, *81*(11), 2563–2591.
- Péré, J. C., B. Bessagnet, M. Mallet, F. Waquet, I. Chiapello, F. Minvielle, V. Pont, and L. Menut (2014), Direct radiative effect of the Russian wildfires and its impact on air temperature and atmospheric dynamics during August 2010, *Atmos. Chem. Phys.*, *14*(4), 1999–2013.
- Pochanart, P. (2003), Carbon monoxide, regional-scale transport, and biomass burning in tropical continental Southeast Asia: Observations in rural Thailand, *J. Geophys. Res.*, *108*(D17), 4552, doi:10.1029/2002JD003360.
- Ramanathan, V., M. V. Ramana, G. Roberts, D. Kim, C. Corrigan, C. Chung, and D. Winker (2007), Warming trends in Asia amplified by brown cloud solar absorption, *Nature*, *448*(7153), 575–575.
- Saide, P., S. Spak, R. Pierce, J. Otkin, T. Schaack, A. Heidinger, A. Silva, M. Kacenelenbogen, J. Redemann, and G. Carmichael (2015), Central American biomass burning smoke can increase tornado severity in the US, *Geophys. Res. Lett.*, *42*, 956–965, doi:10.1002/2014GL062826.
- Stettler, M. E. J., S. Eastham, and S. R. H. Barrett (2011), Air quality and public health impacts of UK airports. Part I: Emissions, *Atmos. Environ.*, *45*(31), 5415–5424.
- Stone, E. A., G. C. Lough, J. J. Schauer, P. S. Praveen, C. E. Corrigan, and V. Ramanathan (2007), Understanding the origin of black carbon in the atmospheric brown cloud over the Indian Ocean, *J. Geophys. Res.*, *112*, D22S23, doi:10.1029/2006JD008118.
- Streets, D. G., K. F. Yarber, J. H. Woo, and G. R. Carmichael (2003), Biomass burning in Asia: Annual and seasonal estimates and atmospheric emissions, *Global Biogeochem. Cycles*, *17*(4), 1099, doi:10.1029/2003GB002040.
- Twomey, S. (1977), Influence of pollution on shortwave albedo of clouds, *J. Atmos. Sci.*, *34*(7), 1149–1152.
- van der Werf, G. R., J. T. Randerson, L. Giglio, G. J. Collatz, M. Mu, P. S. Kasibhatla, D. C. Morton, R. S. DeFries, Y. Jin, and T. T. van Leeuwen (2010), Global fire emissions and the contribution of deforestation, savanna, forest, agricultural, and peat fires (1997–2009), *Atmos. Chem. Phys.*, *10*(23), 11,707–11,735.
- Wang, C., J. J. Corbett, and J. Firestone (2008), Improving spatial representation of global ship emissions inventories, *Environ. Sci. Technol.*, *42*(1), 193–199.
- Wang, J., and S. A. Christopher (2006), Mesoscale modeling of Central American smoke transport to the United States: 2. Smoke radiative impact on regional surface energy budget and boundary layer evolution, *J. Geophys. Res.*, *111*, D14S92, doi:10.1029/2005JD006720.
- Wang, J., S. A. Christopher, U. S. Nair, J. S. Reid, E. M. Prins, J. Szykman, and J. L. Hand (2006), Mesoscale modeling of Central American smoke transport to the United States: 1. “Top-down” assessment of emission strength and diurnal variation impacts, *J. Geophys. Res.*, *111*, D05S17, doi:10.1029/2005JD006416.
- Wang, Y., D. J. Jacob, and J. A. Logan (1998), Global simulation of tropospheric O₃-NO_x-hydrocarbon chemistry: 1. Model formulation, *J. Geophys. Res.*, *103*, 10,713–10,725, doi:10.1029/98JD00158.
- Wang, Y., J. Wang, X. Xu, D. K. Henze, Y. Wang, and Z. Qu (2016), A new approach for monthly updates of anthropogenic sulfur dioxide emissions from space: Application to China and implications for air quality forecasts, *Geophys. Res. Lett.*, *43*, 9931–9938, doi:10.1002/2016GL070204.
- Wang, Y. X. (2004), A nested grid formulation for chemical transport over Asia: Applications to CO, *J. Geophys. Res.*, *109*, D22307, doi:10.1029/2004JD005237.
- Wesely, M. L. (1989), Parameterization of surface resistances to gaseous dry deposition in regional-scale numerical models, *Atmos. Environ.*, *23*(6), 1293–1304.
- Wiedinmyer, C., S. K. Akagi, R. J. Yokelson, L. K. Emmons, J. A. Al-Saadi, J. J. Orlando, and A. J. Soja (2011), The Fire INventory from NCAR (FINN): A high resolution global model to estimate the emissions from open burning, *Geosci. Model Dev.*, *4*(3), 625–641.
- Williams, J. E., M. van Weele, P. F. J. van Velthoven, M. P. Scheele, C. Liousse, and G. R. van der Werf (2012), The impact of uncertainties in African biomass burning emission estimates on modeling global air quality, long range transport and tropospheric chemical lifetimes, *Atmosphere*, *3*(1), 132–163.
- Winker, D., J. Pelon, J. Coakley Jr., S. Ackerman, R. Charlson, P. Colarco, P. Flamant, Q. Fu, R. Hoff, and C. Kittaka (2010), The CALIPSO mission: A global 3D view of aerosols and clouds, *Bull. Am. Meteorol. Soc.*, *91*, 1211–1229.
- Wu, S. L., L. J. Mickley, D. J. Jacob, J. A. Logan, R. M. Yantosca, and D. Rind (2007), Why are there large differences between models in global budgets of tropospheric ozone? *J. Geophys. Res.*, *112*, 1423–1433, doi:10.1029/2006JD007801.
- Xia, X. G., X. M. Zong, Z. Y. Cong, H. B. Chen, S. C. Kang, and P. C. Wang (2011), Baseline continental aerosol over the central Tibetan plateau and a case study of aerosol transport from South Asia, *Atmos. Environ.*, *45*(39), 7370–7378.
- Xin, J., Y. Wang, Y. Pan, D. Ji, Z. Liu, T. Wen, and P. Wang (2015), The campaign on atmospheric aerosol research network of China: CARE-China, *Bull. Am. Meteorol. Soc.*, *96*(7), 1137–1155, doi:10.1175/BAMS-D-14-00039.1.
- Yang, Z., J. Wang, C. Ichoku, E. Hyer, and J. Zeng (2013), Mesoscale modeling and satellite observation of transport and mixing of smoke and dust particles over northern sub-Saharan African region, *J. Geophys. Res. Atmos.*, *118*, 12,139–12,157, doi:10.1002/2013JD020644.

- Yevich, R., and J. A. Logan (2003), An assessment of biofuel use and burning of agricultural waste in the developing world, *Global Biogeochem. Cycles*, *17*(4), 1095, doi:10.1029/2002GB001952.
- Yokelson, R. J., et al. (2013), Coupling field and laboratory measurements to estimate the emission factors of identified and unidentified trace gases for prescribed fires, *Atmos. Chem. Phys.*, *13*(1), 89–116.
- Zhang, F., et al. (2014), Sensitivity of mesoscale modeling of smoke direct radiative effect to the emission inventory: a case study in northern sub-Saharan African region, *Environ. Res. Lett.*, *9*, 075002.
- Zhang, Q., et al. (2009), Asian emissions in 2006 for the NASA INTEX-B mission, *Atmos. Chem. Phys.*, *9*(14), 5131–5153.
- Zhang, X. Y., Y. Q. Wang, T. Niu, X. C. Zhang, S. L. Gong, Y. M. Zhang, and J. Y. Sun (2012), Atmospheric aerosol compositions in China: spatial/temporal variability, chemical signature, regional haze distribution and comparisons with global aerosols, *Atmos. Chem. Phys.*, *12*(2), 779–799, doi:10.5194/acp-12-779-2012.
- Zhu, J., X. Xia, H. Che, J. Wang, J. Zhang, and Y. Duan (2016), Study of aerosol optical properties at Kunming in southwest China and long-range transport of biomass burning aerosols from North Burma, *Atmos. Res.*, *169*, 237–247.